Nanoscale

COMMUNICATION

View Article Online
View Journal | View Issue

Check for updates

Cite this: *Nanoscale*, 2025, **17**, 21463

Received 1st July 2025,
Accepted 18th August 2025

DOI: 10.1039/d5nr02780b

rsc.li/nanoscale

How octopod Mn–Fe oxide nanoparticle tracers minimize relaxation time and enhance MPI resolution

Ashkan Abdibastami,[a] Agus R. Poerwoprajitno,[a] Zeno Rizqi Ramadhan,[b] Saeed Shanehsazzadeh,[c] Andre Bongers,[c] Chelsea Forest,[a] J. Justin Gooding[a] and Richard D. Tilley*[a,b]

Achieving high spatial resolution in magnetic particle imaging (MPI) remains a major challenge in advancing MPI capabilities. In this study, Mn–Fe oxide nanoparticle tracers with octopod morphology were synthesized, showing a 2.3-fold improvement in spatial resolution while maintaining strong signal intensity at higher tracer concentrations. This approach enables high-resolution MPI by minimizing relaxation time through controlled anisotropy.

Introduction

Magnetic particle imaging (MPI) is an emerging molecular imaging technique that utilizes tracer-based detection to directly measure and quantify the magnetization of superparamagnetic iron oxide nanoparticles (SPIONs).[1–10] Improving the spatial resolution and sensitivity of MPI signal requires minimizing the full width at half maximum (FWHM) and maximizing the peak intensity of the tracer response function (dM/dH).[2,11–13,14] The spatial resolution in MPI is strongly influenced by the inherent magnetic properties of tracers, particularly the characteristics of their M–H magnetization curve.[14,15] A steeper M–H curve results in a narrower point spread function (PSF) in x-space.[1,16–18] The design and optimization of magnetic tracers with the narrowest PSF could be advantageous for applications that require exclusively high resolution.[1,2,18,19]

To date, increasing the size of magnetic nanoparticles (NPs) has been one of the most effective strategies for enhancing spatial resolution in MPI, as increased saturation magnetization generally leads to a reduced FWHM of the PSF.[15,17] The spatial resolution is theoretically expected to improve cubically with increasing magnetic core diameter.[17] On the instrument side, resolution can also be improved by increasing the magnetic field gradient strength of the spatial encoding field ($T\ \mu_0\ m^{-1}$).[17] However, both approaches are accompanied by significant limitations. Increasing core size leads to longer magnetic relaxation times of both Néel and Brownian relaxation, resulting in relaxation-induced blurring that undermines resolution gains from increase in volume.[1,2,17,20] Moreover, from an application standpoint, larger tracers often exhibit reduced blood circulation times and limited tissue penetration, diminishing their effectiveness in biological applications.[1,11,21] Increasing the gradient strength only increases resolution linearly and has rigid limitations posed by hardware restrictions, so that gradients beyond $5\ T\ \mu_0\ m^{-1}$ are practically hard to achieve, in-particular in larger systems suitable for clinical applications.[17]

Mechanistically, the magnetic relaxation dynamics of SPIONs strongly depend on their crystalline anisotropy and morphology, which govern the Néel relaxation time (τ_n), a key determinant of spatial resolution in MPI. The Néel relaxation time exponentially depends on the anisotropy energy barrier, defined by the product of the magnetic anisotropy constant (K) and the particle's magnetic volume (V). By introducing manganese ions (Mn^{2+}) into the iron oxide lattice, the crystalline anisotropy constant can be effectively tuned, reducing the energy barrier and accelerating Néel relaxation. This acceleration minimizes relaxation-induced signal blurring, thereby narrowing the PSF without requiring increases in particle size. Moreover, morphological features such as octopod shapes influence local magnetic environments by altering surface spin disorders and anisotropy distributions, further tuning relaxation behavior. These mechanistic insights enable the design of tracers with enhanced MPI spatial resolution through compositional and morphological engineering rather than conventional size modifications.[22–27]

Here, we demonstrate that 25 nm Mn–Fe oxide (Mn_2FeO_4) nanoparticles, composed of 65.4 at% Mn and exhibiting an octopod morphology, achieve a 2.3-fold improvement over the

---

[a] *School of Chemistry, University of New South Wales, Sydney, NSW 2052, Australia. E-mail: r.tilley@unsw.edu.au*
[b] *Electron Microscope Unit, Mark Wainwright Analytical Centre, University of New South Wales, Sydney, NSW 2052, Australia*
[c] *Biological Resources Imaging Laboratory, Mark Wainwright Analytical Centre, University of New South Wales, Sydney, NSW 2052, Australia*

FWHM of commercial PrecisionMRX® iron oxide NPs of the same size. Although this enhancement is accompanied by a reduction in MPI sensitivity, the signal loss can be compensated by increasing tracer concentration.

Results and discussion

Synthesis and structural characterization

Mn–Fe oxide NPs were synthesized *via* thermal decomposition of iron(III) acetylacetonate and manganese(II) acetylacetonate at 295 °C in benzyl ether, using 1,2-hexadecanediol, oleic acid, and oleylamine as surfactants and reducing agents (see Experimental section in the SI). Thermal decomposition was chosen as the synthesis method because it produces uniform nanoparticles and has previously been demonstrated as a scalable approach for large-scale production.[22] The octopod-shaped Mn–Fe oxide NPs formed after 15 minutes of reaction, with an average size of 25 nm, as observed in the transmission electron microscopy (TEM) image in Fig. 1a. High-angle annular dark-field scanning TEM (HAADF-STEM) and energy-dispersive X-ray spectroscopy (STEM-EDX) mapping, shown in Fig. 1b–e, reveal a uniform Mn and Fe distribution throughout the nanoparticles.

The reaction time was extended to 30 and 60 minutes to investigate the time-dependent growth behavior of the NPs. After 30 minutes, the octopod morphology began transitioning into a dendritic branched structure (Fig. S1, SI), which became fully developed by 60 minutes (Fig. 1f). The average particle size increased to approximately 50 nm after 60 minutes of reaction. The HAADF-STEM image and STEM-EDX mapping (Fig. 1g–j) reveal a compositional gradient, with Mn predominantly concentrated in the shell and Fe enriched in the core indicating the formation of Fe core–Mn shell structures, likely due to elemental migration during particle growth. Inductively coupled plasma optical emission spectroscopy (ICP-OES, Table S1) confirms this shift, showing an increase in the Fe : Mn ratio from 0.53 in the 25 nm octopod-shaped Mn–Fe oxide NPs to 0.74 in the 50 nm Fe core–Mn shell NPs.

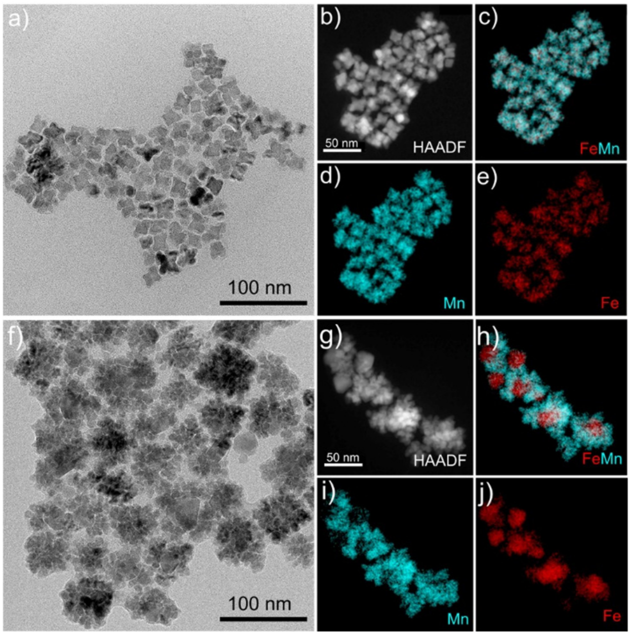

Fig. 1 (a) TEM image of 25 nm octopod-shaped Mn–Fe oxide NPs synthesized after 15 min reaction time, (b) HAADF-STEM image, and (c–e) STEM-EDX maps of Mn/Fe, Mn and Fe. (f) TEM image of 50 nm Fe core–Mn shell NPs formed after a 60 min reaction time, (g) HAADF-STEM image, and (h–j) STEM-EDX maps of Mn/Fe, Mn and Fe.

The time-dependent experiments provide insight into the nanoparticle growth mechanism, which can be categorized into three distinct stages.[28,29] In the initial stage, the formation of Fe and Mn monomers occurs in solution as the temperature is maintained at 200 °C. During the second stage, as the temperature increases to 295 °C, the concentration of Fe and Mn monomers rises, reaching a level of supersaturation.[28] Once the critical supersaturation threshold is exceeded, nucleation begins leading to the formation of NPs with an octopod morphology (Fig. 1a). Nucleation occurs rapidly within the first ~15 minutes at 295 °C, followed by a sharp decrease in monomer concentration due to the burst of nucleation. This reduction suppresses further nucleation and promotes continued growth of the existing NPs. At this stage, the NPs exhibit a uniform alloy-like distribution of Mn and Fe, as evidenced by the compositionally homogeneous octopod Mn–Fe oxide NPs. In the final stage, elemental redistribution occurs, with Fe migrating toward the core and Mn segregating to the shell, resulting in the formation of Fe core–Mn shell structures. The higher Mn-to-Fe ratio observed in initial structures suggests that the Mn precursor decomposes more rapidly than the Fe precursor.

The high-resolution TEM images of the octopod-shaped Mn–Fe oxide NPs and Fe core–Mn shell NPs are shown in Fig. 2a and b, respectively. The octopod-shaped NPs are single crystalline, while the core–shell NPs are polycrystalline. The TEM characterization of PrecisionMRX® iron oxide NPs is shown in Fig. S2, revealing a single-crystal structure with an average particle size of 25 nm. The crystal structure of the NPs was confirmed through selected-area electron diffraction patterns (SAED), as shown in Fig. 2c and d. For both octopod-shaped MnFe oxide NPs and Fe core–Mn shell NPs, the SAED rings matched well with Mn_2FeO_4, confirming the spinel structure. The interplanar spacing (d) values measured for each diffraction ring were in good agreement with the characteristic values for Mn_2FeO_4, corresponding to crystal planes with Miller indices (111), (220), (311), (400), (422), (511), and (440) with d-values of 4.97, 2.99, 2.57, 2.18, 1.75, 1.65, and 1.55 Å, respectively. The fast Fourier transform (FFT) of the high-resolution TEM images in Fig. 2e and f exhibit the characteristic pattern of the Mn_2FeO_4 crystal structure, viewed along the (400) and (220) directions for octopod-shaped Mn–Fe oxide NPs, as well as the (400) and (311) directions for Fe core–Mn shell NPs.

The synthesis approach presented in this study produced octopod-shaped Mn–Fe oxide NPs with high uniformity in size

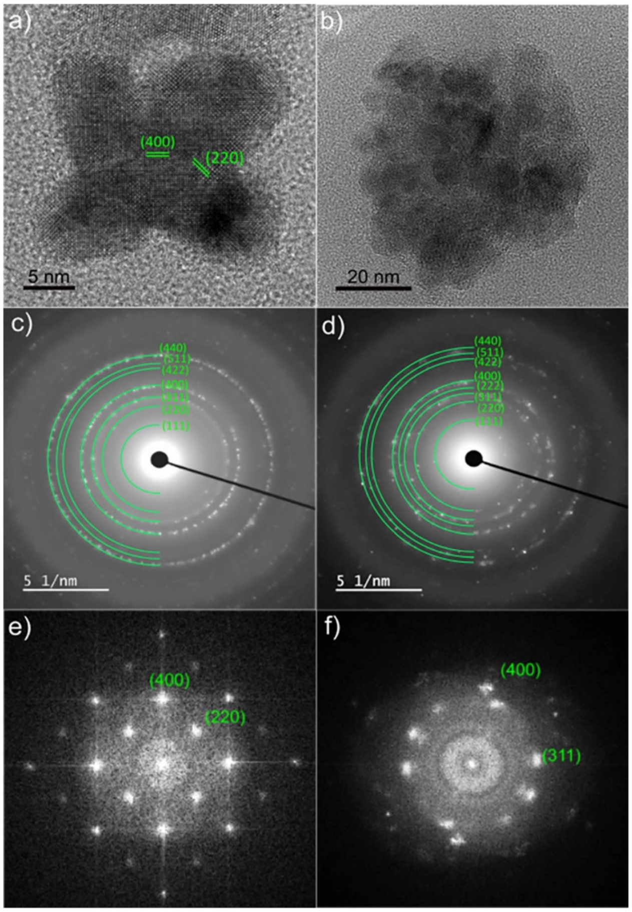

Fig. 2 High-resolution TEM images of (a) 25 nm octopod-shaped Mn–Fe oxide NPs and (b) 50 nm Fe core–Mn shell NPs and their corresponding (c–d) SAED and (e–f) FFT analyses.

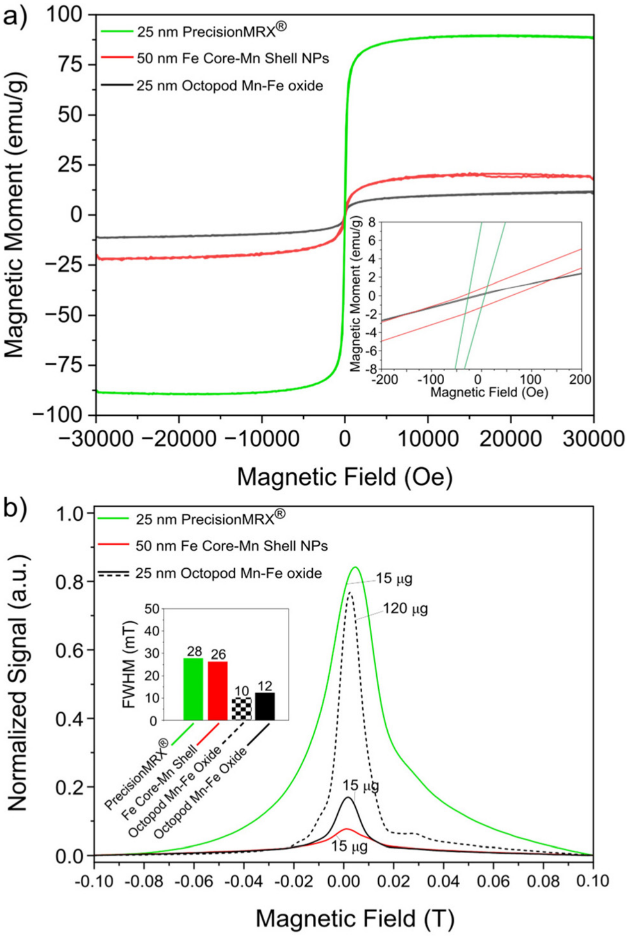

Fig. 3 (a) The field-dependent magnetization curves and (b) the corresponding normalized PSF for 25 nm octopod-shaped Mn–Fe oxide NPs, 50 nm Fe core–Mn shell NPs, and 25 nm commercial PrecisionMRX® iron oxide NPs. Relaxometry measurements were conducted at a sample concentration of 15 μg of total Fe and Mn per 1 mL solvent, except for the hatched graph, which represents signal data for 25 nm octopod Mn–Fe oxide NPs at a concentration of 120 μg of total Fe and Mn per 1 mL solvent.

and shape, a level of uniformity previously achieved only for iron oxide NPs.[30] The nanoparticle morphology remained stable after one year of storage (Fig. S3, SI). The unique crystal structure, shape, and size of these particles, in contrast to Fe core–Mn shell NPs, offer an opportunity to study their magnetic properties and potential applications in MPI.

Magnetic characterization

To evaluate the magnetic properties of the NPs, hysteresis loops were recorded at 300 K using a vibrating sample magnetometer (VSM), as shown in Fig. 3a. The 25 nm commercial PrecisionMRX® iron oxide NPs displayed a high M_{sat} of 90 emu $\mathrm{g_{Fe}}^{-1}$, indicative of a strong alignment of magnetic moments in the applied field. Their low coercivity (16 Oe) and high magnetic susceptibility (0.197 emu Oe^{-1}) confirm superparamagnetic behavior, making them highly responsive to external magnetic fields. In comparison, the 25 nm octopod-shaped Mn–Fe oxide NPs exhibited a much lower M_{sat} of approximately 12 emu $\mathrm{g_{Fe+Mn}}^{-1}$ and a magnetic susceptibility of 0.013 emu Oe^{-1}, with negligible coercivity close to 0. The 50 nm Fe core–Mn shell NPs slightly improved M_{sat} to 20 emu $\mathrm{g_{Fe+Mn}}^{-1}$, with a coercivity of 50 Oe and a magnetic susceptibility of 0.019 emu Oe^{-1}.

To further understand the magnetic behavior of Mn–Fe oxide NPs, zero-field-cooled (ZFC) and field-cooled (FC) cycles were measured using a VSM. The ZFC/FC curve (Fig. S4, SI) of the 25 nm octopod-shaped Mn–Fe oxide NPs shows a significantly lower blocking temperature (T_{b}) of around 125 K, in contrast to the 50 nm Fe core–Mn shell NPs with a T_{b} of approximately 275 K. The low T_{b} of the octopod-shaped sample reflects its superparamagnetic behavior at room temperature, attributed to reduced crystalline anisotropy resulting from the Mn–Fe oxide spinel structure and its unique octopod morphology. In contrast, Fe core–Mn shell NPs exhibit a broad cusp in the ZFC curve, reflecting a wider particle size and anisotropy distribution, which results in a less uniform magnetic response. The separation between ZFC/FC curves also highlights interparticle interactions and differences in magnetic relaxation dynamics among the samples, with the 25 nm octopod-shaped Mn–Fe oxide NPs exhibiting minimal separation, indicative of negligible magnetic retention and reduced interparticle interactions.

MPI measurement

The MPI performance of the samples, at a concentration of 15 μg of magnetic atoms per mL *n*-hexane, was evaluated using a preclinical Magnetic Insight Momentum MPI scanner. Fig. 3b shows the normalized PSF obtained from relaxometry measurements. Spatial resolution was assessed by measuring the FWHM of the PSF, representing image blurring caused by particle relaxation (Table 1). Among the samples, the 25 nm octopod-shaped Mn–Fe oxide NPs demonstrated the narrowest FWHM of 12 mT (~2.1 mm), offering the highest spatial resolution, which is approximately 2.1–2.3 times greater than that of commercial PrecisionMRX® (28 mT FWHM, ~4.9 mm) and Fe core–Mn shell NPs (26 mT FWHM, ~4.5 mm). This enhanced resolution is attributed to the lower crystalline anisotropy of the octopod-shaped NPs, which reduces the Néel time constant and enables faster magnetic relaxation.[2,17,26] Brownian relaxation is less likely to contribute significantly in octopod-shaped NPs, as the faster Néel relaxation ensures that the magnetic moments flip before any physical rotation of the NPs occurs.[17]

The signal sensitivity (maximum peak intensity) of the octopod-shaped and core–shell NPs was significantly lower compared to the commercial PrecisionMRX®, with reductions of 5-fold and 12-fold (Fig. 3b), respectively. This is due to their low M_{sat} (Fig. 3a), which results from high Mn substitution introducing antiferromagnetic interactions within the lattice, thereby weakening the net magnetic moment. The loss in peak signal intensity for the 25 nm octopod Mn–Fe oxide NPs was offset by increasing the tracer concentration from 15 μg mL^{-1} to 120 μg mL^{-1}, resulting in a comparable to that of commercial PrecisionMRX®, while still maintaining superior resolution (Table 1). This adjustment achieved a balance between resolution and signal strength, as illustrated by the bar graph in Fig. 3b.

The reduced crystalline anisotropy lowers the energy barrier for magnetic moment reorientation, allowing for faster and more coherent magnetic response under the oscillating magnetic field used in MPI. Combined with the shorter Néel relaxation time, this enables more efficient magnetization reversal, improving the signal response and sensitivity of the nanoparticles. These effects collectively enhance the MPI performance compared to commercial systems. Magnetic properties are affected by morphology, composition, crystal structure, and nanoparticle size.[21,31] The octopod-shaped manganese-iron oxide nanoparticles are well-suited for use as MPI tracers because they have a single crystal structure and a small size of 25 nanometers.

Table 1 Summary of relaxometry MPI signal data

Sample	Total μg (Fe, Mn)	FWHM (mT)	Resolution (mm)	Max PSF (a.u.)
Octopod Mn–Fe oxide NPs	15	12	2.1	0.17
	120	10	1.7	0.76
Fe core–Mn shell NPs	15	26	4.5	0.07
PrecisionMRX®	15	28	4.9	0.84

Conclusions

In conclusion, this study highlights the potential of Mn–Fe oxide NPs with optimized morphology and composition to improve resolution in MPI. The 25 nm octopod-shaped Mn–Fe oxide NPs exhibited a significant reduction in FWHM of the PSF signal to 12 mT, corresponding to a 2.3-fold improvement in resolution compared to the 28 mT FWHM of the commercial PrecisionMRX® iron oxide NPs and significantly better than the 26 mT FWHM of the Fe core–Mn shell NPs. This improvement is attributed to their reduced crystalline anisotropy and shorter Néel relaxation time. This demonstrates that spatial resolution can be controlled by modifying tracer morphology and composition to affect crystalline anisotropy and hence relaxation dynamics, which offers an additional parameter for fine-tuning MPI tracer performance to optimize MPI tracer performance beyond the well-established parameters such as particle size and magnetic susceptibility. The trade-off of introducing antiferromagnetic interactions into NPs is of course a reduced M_{sat} which led to significant reduction in signal peak intensity compared to the pure iron oxide sample (PrecisionMRX®). However, in many practical experiments this limitation can be offset by increasing the tracer concentration by 8 times. These findings underscore the trade-offs between spatial resolution and sensitivity in MPI tracers, highlighting the potential of octopod-shaped Mn–Fe oxide NPs for applications requiring exceptionally high resolution. This work opens opportunities for *in vivo* validation and for extending the synthetic approach to other dopant systems, thereby broadening its applicability and potential impact.

Author contributions

The manuscript was written through contributions of all authors. All authors have given approval to the final version of the manuscript.

Conflicts of interest

There are no conflicts to declare.

Data availability

The data supporting this article have been included as part of the SI. The supplementary information includes TEM images, statistical distributions, EDS mappings, and ZFC/FC magnetization curves. See DOI: **https://doi.org/10.1039/d5nr02780b**.

Acknowledgements

This work was supported by the Australian Research Council's Discovery Project grants awarded to R. D. T. (DP230100596, DP250100915, IC210100056 and CE230100032) and J. J. G. (DP210102698). We acknowledge support from Microscopy Australia, the National Imaging Facility, Australia, as well as the Mark Wainwright Analytical Center, the Biological Resources Imaging Laboratory UNSW and the Electron Microscope Unit at the University of New South Wales. This work was performed, in part, at the Center for Integrated Nanotechnologies.

References

1 H. T. K. Duong, A. Abdibastami, L. Gloag, L. Barrera, J. J. Gooding and R. D. Tilley, *Nanoscale*, 2022, **14**, 13890–13914.
2 C. Lu, L. Han, J. Wang, J. Wan, G. Song and J. Rao, *Chem. Soc. Rev.*, 2021, **50**, 8102–8146.
3 B. Gleich and J. Weizenecker, *Nature*, 2005, **435**, 1214–1217.
4 P. Szwargulski, N. Gdaniec, M. Graeser, M. Möddel, F. Griese, K. M. Krishnan, T. M. Buzug and T. Knopp, *J. Med. Imag.*, 2018, **5**(4), 046002.
5 A. C. Velazquez-Albino, A. Nozka, A. Melnyk, H. J. Good and C. M. Rinaldi-Ramos, *ACS Appl. Nano Mater.*, 2024, **7**, 279–291.
6 J. Guzy, S. Chakravarty, F. J. Buchanan, H. Chen, J. M. Gaudet, J. M. L. Hix, C. L. Mallett and E. M. Shapiro, *ACS Appl. Nano Mater.*, 2020, **3**, 3991–3999.
7 L.-M. Lacroix, D. Ho and S. Sun, *Curr. Top. Med. Chem.*, 2010, **10**, 1184–1197.
8 Q. A. Pankhurst, N. K. T. Thanh, S. K. Jones and J. Dobson, *J. Phys. D: Appl. Phys.*, 2009, **42**, 224001.
9 L. Gloag, M. Mehdipour, M. Ulanova, K. Mariandry, M. A. Nichol, D. J. Hernández-Castillo, J. Gaudet, R. Qiao, J. Zhang, M. Nelson, B. Thierry, M. A. Alvarez-Lemus, T. T. Tan, J. J. J. Gooding, N. Braidy, P. S. Sachdev and R. D. Tilley, *Chem. Commun.*, 2020, **56**, 3504–3507.
10 H. Arami, E. Teeman, A. Troksa, H. Bradshaw, K. Saatchi, A. Tomitaka, S. S. Gambhir, U. O. Häfeli, D. Liggitt and K. M. Krishnan, *Nanoscale*, 2017, **9**, 18723–18730.
11 A. Abdibastami, L. Gloag, J. P. Prada, H. Thien, K. Duong, S. Shanehsazzadeh, S. A. Sulway, S. Cheong, H. Hackbarth, N. M. Bedford, G. N. L. Jameson, A. Bongers, J. J. Gooding and R. D. Tilley, *Chem. Mater.*, 2024, **36**, 8773–8781.
12 L. M. Bauer, S. F. Situ, M. A. Griswold and A. C. S. Samia, *Nanoscale*, 2016, **8**, 12162–12169.
13 S. Harvell-Smith, L. D. Tunga and N. T. K. Thanh, *Nanoscale*, 2022, **14**, 3658.
14 R. Hufschmid, J. Landers, C. Shasha, S. Salamon, H. Wende and K. M. Krishnan, *Phys. Status Solidi A*, 2019, **216**, 1–8.
15 C. Shasha, E. Teeman and K. M. Krishnan, *Biomed. Phys. Eng. Express*, 2019, **5**, 055010.
16 N. Panagiotopoulos, R. L. Duschka, M. Ahlborg, G. Bringout, C. Debbeler, M. Graeser, C. Kaethner, K. Lüdtke-Buzug, H. Medimagh, J. Stelzner, T. M. Buzug, J. Barkhausen, F. M. Vogt and J. Haegele, *Int. J. Nanomed.*, 2015, **10**, 3097–3114.
17 Z. W. Tay, D. W. Hensley, E. C. Vreeland, B. Zheng and S. M. Conolly, *Biomed. Phys. Eng. Express*, 2017, **3**, 035003.
18 K. L. B. Fung, C. Colson, J. Bryan, C. Saayujya, J. Mokkarala-Lopez, A. Hartley, K. Yousuf, R. Kuo, Y. Lu, B. D. Fellows, P. Chandrasekharan and S. M. Conolly, *Nano Lett.*, 2023, **23**, 1717–1725.
19 A. J. McGrath, S. Cheong, A. M. Henning, J. J. Gooding and R. D. Tilley, *Chem. Commun.*, 2017, **53**, 11548–11551.
20 G. Barrera, P. Allia and P. Tiberto, *ACS Appl. Nano Mater.*, 2022, **5**, 2699–2714.
21 H. T. K. Duong, A. Abdibastami, L. Gloag, A. Bongers, S. Shanehsazzadeh, M. Nelson, A. Cousins, N. Bayat, H. McCalmont, R. B. Lock, S. Sulway, J. Biazick, J. J. Gooding and R. D. Tilley, *J. Magn. Magn. Mater.*, 2023, **587**, 171304.
22 J. Park, K. An, Y. Hwang, J.-G. Park, H.-J. Noh, J.-Y. Kim, J.-H. Park, N.-M. Hwang and T. Hyeon, *Nat. Mater.*, 2004, **3**, 891–895.
23 M. F. Casula, E. Conca, I. Bakaimi, A. Sathya, M. E. Materia, A. Casu, A. Falqui, E. Sogne, T. Pellegrino and A. G. Kanaras, *Phys. Chem. Chem. Phys.*, 2016, **18**, 16848–16855.
24 G. Maties, M. Luu, K. Ait-Oukaci, I. Lecerf, C. Marcelot, A. Fondet, S. Cayez, C. Gatel, T. Blon, B. Chaudret and L. M. Lacroix, *J. Phys. Chem. C*, 2022, **126**, 20668–20677.
25 B. Mehdaoui, A. Meffre, L.-M. Lacroix, J. Carrey, S. Lachaize, M. Respaud, M. Gougeon and B. Chaudret, *J. Appl. Phys.*, 2010, **107**, 09A324.
26 L. H. Nguyen, P. T. Phong, P. H. Nam, D. H. Manh, N. T. K. Thanh, L. D. Tung and N. X. Phuc, *Materials*, 2021, **14**, 1875.
27 H. T. K. Duong, A. R. Poerwoprajitno, A. Bongers, S. Shanehsazzadeh, A. Abdibastami, S. Sulway, A. Rich, J. J. Gooding and R. D. Tilley, *J. Phys. Chem. B*, 2025, **129**, 1774–1783.
28 N. T. K. Thanh, N. Maclean and S. Mahiddine, *Chem. Rev.*, 2014, **114**, 7610–7630.
29 J. Ren and R. D. Tilley, *J. Am. Chem. Soc.*, 2007, **129**, 3287–3291.
30 Z. Nemati, J. Alonso, L. M. Martinez, H. Khurshid, E. Garaio, J. A. Garcia, M. H. Phan and H. Srikanth, *J. Phys. Chem. C*, 2016, **120**, 8370–8379.
31 A. R. Poerwoprajitno, N. Baradwaj, M. K. Singh, C. B. Carter, D. L. Huber, R. Kalia and J. Watt, *J. Phys Mater.*, 2023, **6**, 045013.